# Microscale Silicon Origami

Zeming Song, Cheng Lv, Mengbing Liang, Varittha Sanphuang, Kedi Wu, Bin Chen, Zhi Zhao, Jing Bai, Xu Wang, John L. Volakis, Liping Wang, Ximin He, Yu Yao, Sefaattin Tongay, and Hanqing Jiang*

Origami, originally the art of paper folding, is becoming a source of inspiration for science and engineering in recent years. Utilizing the principles of origami, namely, creation of three dimensional (3D) structures from two dimensional (2D) sheets and tunability of the folded structures, various breakthroughs are facilitated, including a concept model in cosmology,[1] Deoxyribose Nucleic Acid (DNA) structures,[2–4] foldable and stretchable electronics,[5–8] and a framework of metamaterial.[9,10] One particularly interesting application of origami is to form complicated 3D architectures from 2D sheets, which paves a way to fabricate complex 3D patterns that are otherwise impossible. The applications of 3D architectures span from many disciplines. Specifically in microscale regimes, there are 3D micro-electromechanical systems (MEMS),[11,12] artificial biological systems,[13,14] metrology,[15,16] and energy storages.[17] Some strategies have been developed to fabricate microscale 3D structures, such as self-assembly[18] and residual stress-induced bending[19] that are limited to choices of materials. A recent compressive buckling[20] approach is capable to fabricate 3D structures while the shape of which is only limited to ribbon-liked one. The similar approach was extended to thin-film configurations to make 3D structures,[21,22] though cutting and/or pre-patterned creases are still used. Other approaches involve the capillary[23,24] force driven self-folding mechanism at creases to generate millimeter scale origami, which has limitations to make periodic arrays of origami patterns or microscale origami patterns due to the application of the capillary force. Grain coalescence[25] has been utilized to make nanometer-scale origami patterns, though this approach involves complicated controls and thus limits their applications. A recent review also summarized some of the existing approaches on fabrication of 3D structures.[26]

The intrinsic geometrical feature of origami, i.e., high aspect ratio between the out-of-plane dimension of the origami (vertical distance from the "mountain" vertex to the "valley" vertex) and thickness of 2D sheets, which is typically much greater than 100 nm, makes the widely used fabrication approaches, such as photolithography and 3D printing, incapable for manufacture of microscale origami. Here, we demonstrate a new strategy to fabricate microscale origami using Si nanomembranes (NMs) as the materials which are supported by elevated polydimethylsiloxane (PDMS) walls on top of a PDMS substrate. Thus the Si NMs are suspended. Upon relaxation of the pre-stretch applied on the PDMS substrates, the suspended Si NMs buckle with the pre-patterned wall as the support and constraints to form designated microscale Si origami. Thus, the final microscale origami patterns are controlled by the patterning of the elevated wall. Because of the microscale characteristics of the origami architectures and the continuum feature of the NMs, the microscale origami may lead to multiple breakthroughs, such as in electromagnetics. In this paper, we showed one application of the fabricated microscale Si NM origami as reconfigurable antenna in the THz regime. Other potential applications include microscale grating, thermal invisible device, and low observable (stealth) structures. This approach is different and complementary to the recent compressive buckling approach[20–22] as it enables the formation of periodic microscale origami patterns using uncut and unpatterned Si NMs.

The methodology is illustrated in **Figure 1**a. An elastomeric substrate PDMS (Sylgard 184, Dow Corning) is mold cast to a shape with pre-patterned, elevated walls on top of a stab, followed by biaxial or uniaxial pre-stretch (from $L$ to $L + \Delta L_1$ and $L + \Delta L_2$ along the two perpendicular in-plane directions), which can be achieved by mechanical means or heating. The characteristic sizes of the elevated walls are on the order of 10–200 μm. The pre-stretched PDMS is subjected to ultraviolet/ozone treatment in order to form activated hydroxyl groups for bonding. Because the PDMS walls are elevated, they thus provide selective bonding sites. Then an

Dr. Z. Song, Dr. C. Lv, K. Wu, B. Chen, Dr. Z. Zhao,
X. Wang, Prof. L. Wang, Prof. X. He, Prof. S. Tongay,
Prof. H. Jiang
School for Engineering of Matter, Transport and Energy
Arizona State University
Tempe, AZ 85287, USA
E-mail: hanqing.jiang@asu.edu

M. Liang, J. Bai, Prof. Y. Yao
School of Electrical
Computer and Energy Engineering
Arizona State University
Tempe, AZ 85287, USA

V. Sanphuang, Prof. J. L. Volakis
ElectroScience Laboratory
Department of Electrical and Computer Engineering
The Ohio State University
Columbus, OH 43212, USA

Prof. H. Jiang
MOE Key Lab of Disaster Forecast and Control in Engineering
Jinan University
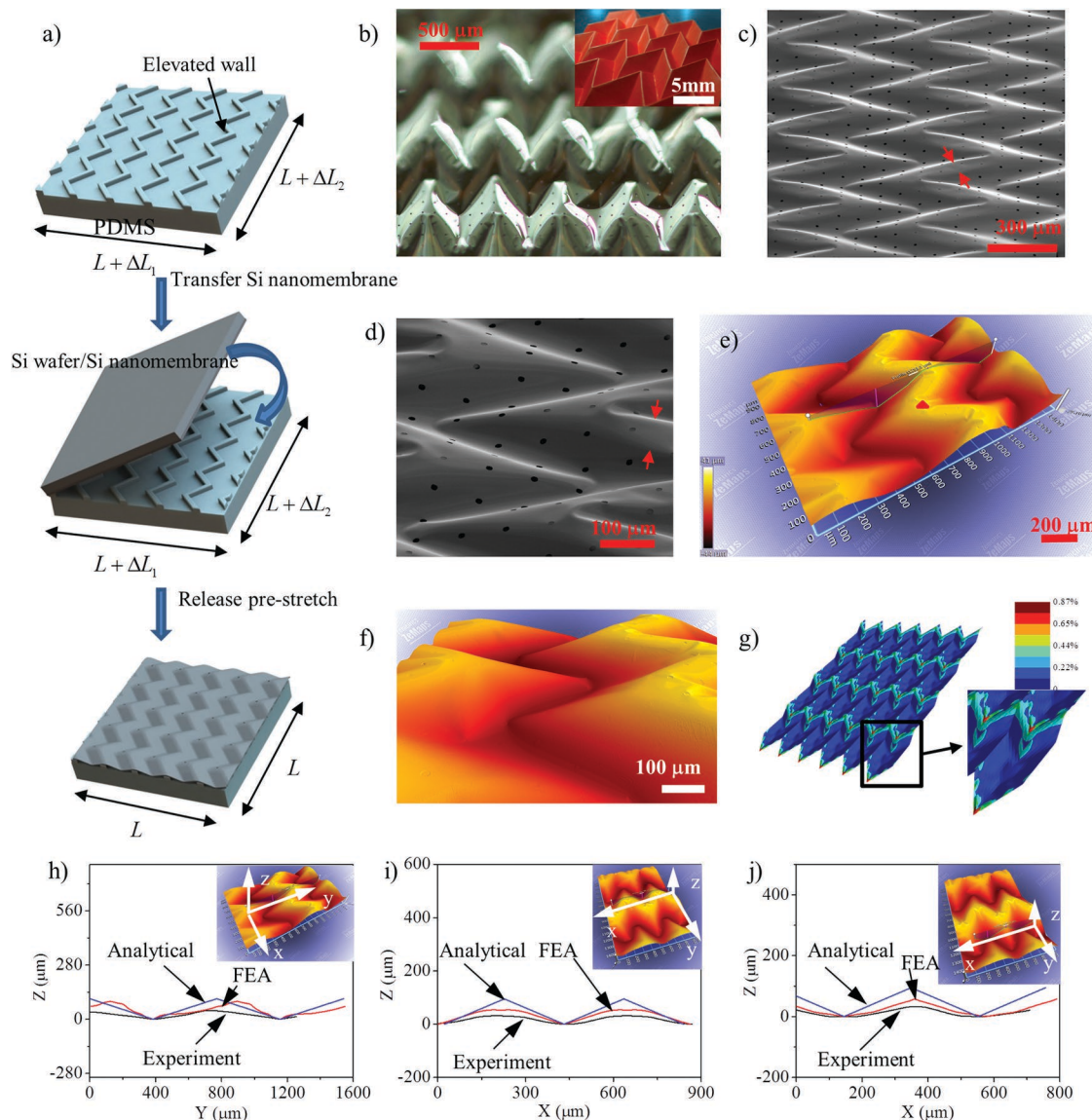Guangzhou 510632, China

DOI: 10.1002/smll.201601947

**Figure 1.** Forming a silicon (Si) nanomembrane (NM) origami pattern. a) Schematic illustration of using elevated PDMS walls to suspend Si NM and releasing the pre-stretch to generate designated microscale origami patterns. Here, the elevated PDMS walls have been pre-patterned for the Miura-ori pattern. b) A photography of an Si NM Miura-ori pattern. The inset shows a paper-based Miura-ori pattern for comparison. c) A scanning electron microscopy (SEM) image shows periodic Si NM Miura-ori pattern in an overall 1 mm × 1 mm area. d) An SEM image shows the details of the Si NM Miura-ori pattern. e) An optical profilometer image shows the Si NM Miura-ori pattern. The line cut measurement was performed. f) An optical profilometer image shows the details of the Si NM Miura-ori pattern. g) Finite element analysis (FEA) results of Si NM Miura-ori pattern. The contour plot is for the principal stress of buckled Si NM. h–j) Line cut comparisons between the experiment, FEA, and analytical solution. The inset shows an image of optical profilometer, in which the line cut profile was measured in experiment. The measured directions are: h) "mountain"–"valley"–"mountain" cut along *y*-direction, i) along the mid-point of "mountain" creases, and j) "mountain"–"valley"–"mountain" cut along *x*-direction.

Si NM, derived from the device layer of a silicon-on-insulator (SOI) wafer, is brought to contact with the patterned PDMS. Specifically, the elevated PDMS walls provide supports to Si NM and thus Si NM is suspended. Because of the surface treatment, condensation reactions occur at room temperature between the elevated PDMS walls and the native oxide surfaces of Si NMs.[27–29] Si NMs then can be exfoliated from the SOI wafer and adhered to the elevated PDMS walls. The detailed processes are provided in the Experimental Section. Once the pre-stretch exceeds a certain critical level, relaxation of the pre-stretch suspended Si NMs enables its buckling and forms origami patterns. The buckling is the result

of releasing the membrane energy through the out-of-plane deformation via mainly bending and sometime twisting. The resulted origami patterns are defined by two factors: (1) the shape of the pre-patterned, elevated walls, and (2) the nature of pre-stretch (i.e., biaxial with different pre-stretches in two directions vs equi-biaxial pre-stretch). The first factor determines the type of the origami and later tunes the patterns.

As a specific example using the pre-patterned walls with shapes illustrated in Figure 1a, a Miura-ori pattern[30] can be obtained. Figure 1b shows a photography of an Si NM Miura-ori pattern generated using this approach, where the thickness of the Si NM is 300 nm and the equi-biaxial pre-strain of

3.6% was introduced by heating the PDMS from room temperature to 120 °C. Video S1 (Supporting Information) shows the buckling process as the temperature drops from 120 °C to room temperature. The detailed geometry of the pre-patterned PDMS wall is given in Figure S1a,b (Supporting Information). It is apparent that in a 2.2 mm × 2.2 mm area this Si NM Miura-ori pattern replicates the paper-based Miura-ori, given by the inset of Figure 1b. The observable difference is that the sharp "mountain" creases in paper-based Miura-ori are replaced by the flat PDMS walls in the Si NM Miura-ori, because the downward out-of-plane buckling occurs and the elevated PDMS walls actually serve as "mountain" supports for the Si NMs. The "valley" creases are not as sharp as paper-based pattern because of the much lower energy state of relative smooth crease is usually preferred. It is emphasized here that using this origami inspired methodology, a planar structure is transferred to a 3D architecture across an entirely continuum film, rather than discretized ribbons.[20] Figure 1c,d shows the scanning electron microscopy (SEM) images of the Si NM Miura-ori patterns, where the well-defined periodicity is clearly observed. The measured width of the PDMS wall is about 117.02 µm (shown within red arrows in Figure 1c,d), which is larger than the pre-designed 111.8 µm (Figure S1b, Supporting Information) due to partial delamination at the wall. Figure S1c,d (Supporting Information) provides a cross-sectional view near the elevated PDMS walls using an integrated focused ion beam (FIB) and an SEM system, where the partial delamination is observed at the vertices of the elevated PDMS walls. The partial delamination may release the stress concentration at the wall. Figure 1e,f provides the optical profilometer images of the Si NM Miura-ori pattern. It is observed that the Si NM has apparent deformation at the vertices of the elevated wall (marked by the red triangle) in Figure 1e, which suggests a localized and possibly large strain. To compare the experiments with calculated stress and strain during buckling, finite element analysis (FEA) was conducted. A unit cell of the Si NM is simulated in the FEA (Figure S2a,b, Supporting Information), which consists of four parallelograms. For simplicity, PDMS walls are not explicitly included and just implicitly appear as boundary conditions to the Si NMs. Details of the FEA are provided in the Supporting Information. Using the equi-biaxial pre-strain of 3.6%, the FEA results (Figure 1g) show a simulated Miura-ori pattern with good agreement with that observed in experiments. The good alignment between FEA and experiments suggests that FEA can be utilized to design the origami patterned generated by buckling. FEA results show that the maximum principal strain 0.87% appears at the vertex of the "mountain" creases, which is less than the 1% fracture strain of single crystalline Si. Figure 1h–j shows the line-cut comparison between the experiments, FEA results, and analytical expression of rigorous Miura-pattern. For Miura-ori pattern, the closed loop solution can be obtained (detailed in the Supporting Information) because it has only one degree of freedom. Use $n$ to denote the number of creases at one vertex and thus $n = 4$ for Miura-ori. For ideally rigid origami (e.g., Miura-ori) where all facets are rigid and only the creases deform during folding, it is known that there are $n − 3$ degrees of freedoms;[31,32] thus Miura-ori has only one

degree of freedom. It is observed that the generated Si NM origami agrees reasonably well with both the analytical and FEA results. The major discrepancies occur at the "mountain" vertices since the analytical solution and FEA results are based on zero size of creases while the experiments have finite size of the elevated PDMS walls.

Wide range and more complicated Si NM origami patterns can be realized, with the inspiration from the paper-based origami. The logic is to vary the shape of the elevated PDMS walls. As there are significant variations of paper-based origami, the first extension from Figure 1b (Miura-ori with one degree of freedom) is an origami pattern with three degrees of freedoms. **Figure 2**a shows a photography of an Si NM origami with waterbomb pattern, or the nickname "magic ball" pattern, through the relaxation of equi-biaxial 3.6% pre-strain via thermal expansion of the PDMS. The detailed shape and geometry of the elevated PDMS walls to form this pattern are given in the Figure S3a,b (Supporting Information). Great similarity is observed when compared with the paper-based "magic ball" pattern (inset of Figure 2a). However, a discrepancy is also noticed and in fact related to the methodology of generating microscale origami using elevated PDMS walls. For ideal "magic ball" pattern (as detailed in the Supporting Information), the "mountain" creases always form a curved geometry and cannot stay flat unless at the completed collapsed state, which is different from the Si NM origami (Figure 2a) where the "mountain" creases (i.e., elevated PDMS walls) are on the flat state. The reason is that Si NM is not ideal rigid and facets are allowed to deform. To characterize the localized strain due to the deformation of Si NMs, Raman spectroscopy was conducted. At a vertex of the "mountain" crease, there are six creases intersecting. It is thus expected to have the maximum strain. As seen from Figure 2b, the strain mapping of the Si NM "magic ball" patterns near a vertex of the "mountain" crease shows that the maximum localized strain is about 0.1%, much less than the commonly taken fracture strain of single crystalline Si of 1%. More details about Raman spectroscopy measurements are provided in Figure S5a,b (Supporting Information). Figure 2c,d further shows the SEM and optical profilometer of Si NM "magic ball" patterns. This demonstration suggests that this methodology is able to mimic paper-based origami with complicated shapes and further modify them by utilizing the deformability of Si NMs.

Figure 2e,f provides more Si NM origami patterns that, by theory,[31,32] cannot be rigidly folded while can be achieved using the present methodology. Figure 2e presents the photography of a non-rigidly foldable pattern using staggered PDMS walls given in Figure S6a,b (Supporting Information). To generate this pattern, Si NMs have to be geometrically compatible at the facets through bending, which can be clearly observed in Figure 2f (optical profilometer). Very sharp creases are observed. Related to this pattern that it is not rigid foldable at all vertices, some patterns are rigid foldable at the unit cell level but not at the assembled level, such as the star pattern shown in Figure 2g–i. The shape and geometry of the PDMS walls are given in Figure S7a,b (Supporting Information). In this pattern, the unit cell is a star, which is rigid foldable. However, when two stars are
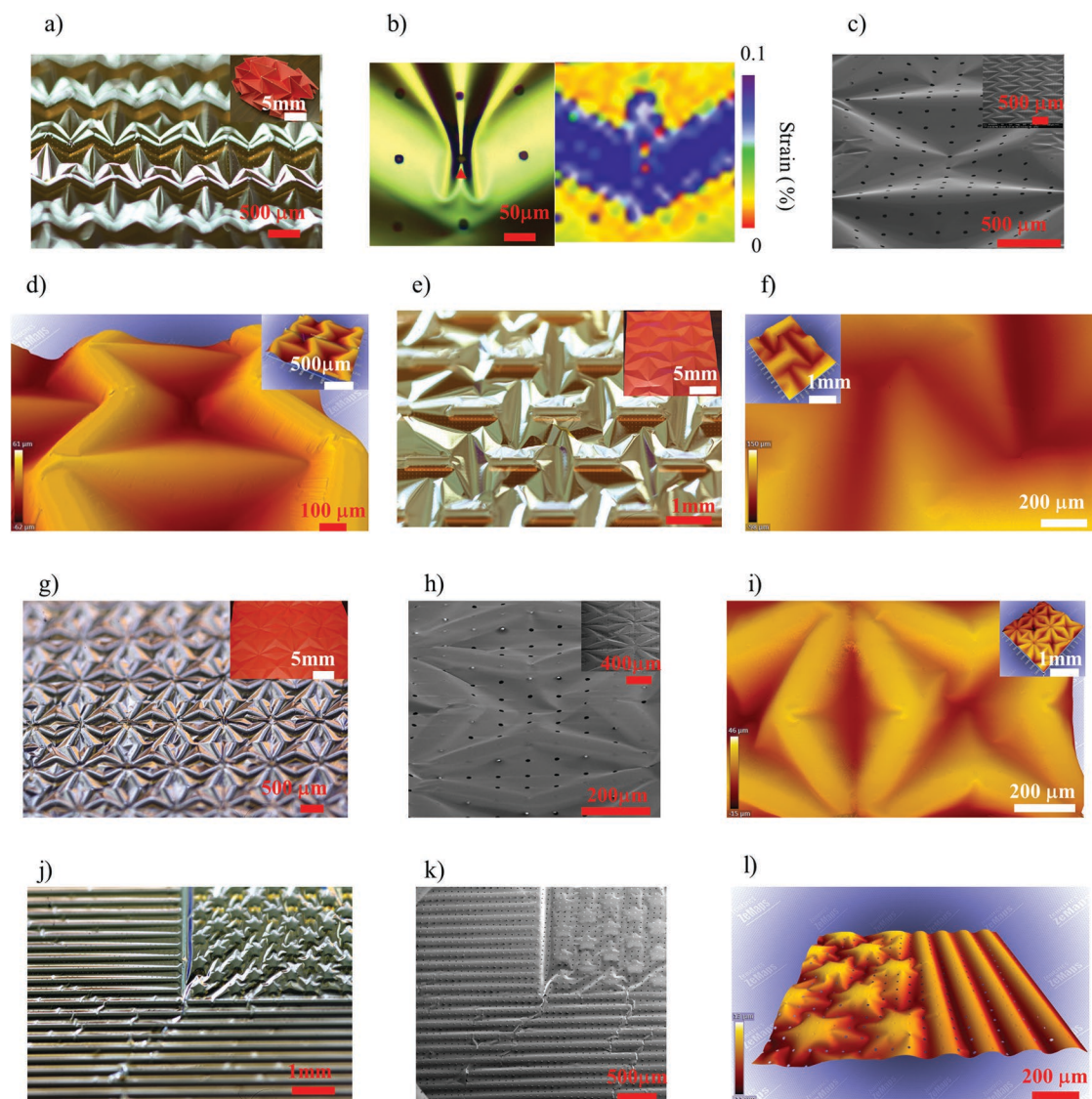
**Figure 2.** Demonstration of other silicon (Si) nanomembrane (NM) origami patterns with different characteristics. a) A photography of an Si NM "magic ball" pattern. The inset shows a paper-based Miura-ori pattern for comparison. b) Optical image of the region near the exceedingly bended tip, which is marked by a red triangle. Strain mapping of an Si NM "magic ball" pattern as calculated from Raman spectroscopy measurement. c) A scanning electron microscopy (SEM) image shows Si NM "magic ball" pattern in an overall 0.7 mm × 0.7 mm area. d) An optical profilometer image shows the Si NM "magic ball" pattern. The line cut measurement was performed. e) A photography of an Si NM non-rigidly foldable pattern. f) A optical profilometer image shows the Si NM non-rigidly foldable pattern. g) A photography of an Si NM star pattern. h) An SEM image shows Si NM star pattern. i) A optical profilometer image shows the Si NM star pattern. j) A photography of an Si NM US Flag pattern. k) An SEM image shows Si NM US Flag pattern. l) An optical profilometer image shows the Si NM US Flag pattern.

assembled, their boundaries are not compatible. Composite and non-periodic patterns can be generated by combing multiply patterns, such as the mimicked US Flag shown in Figure 2j–l consisting of stars and stripes. Detailed shape and geometry of US Flag pattern are given in the Figure S8a–c (Supporting Information).

The great tunability of origami and the microscale feature size of Si NM origami provide unexplored applications on reconfigurable antenna in the THz regimes. Sample was prepared using Si origami with magic ball structure as shown in **Figure 3**a. It was fabricated by depositing 300 nm thick gold layer on part of Si NMs where was supported by PDMS walls and 150 µm wide, 300 nm thick gold strips between those zigzag shape gold layers. The transmissions of the sample are

measured using THz-TDS transmission gantry.[33] Principle of instrument was introduced in Figure S9 (Supporting Information). The gold pattern structure printed on this structure is resonated at 0.059 THz as plotted in Figure 3b. The transmission peak provides more than 80% at room temperature (24 °C). While heating up the origami structure, the depth of Si is changed (Si membrane is stretched) as in the direction of incident wave. Therefore, the transmission peak increases from 82% to 90% when the temperature increases up to 120 °C as shown in Figure 3c.

In this paper, we reported a new methodology to create 3D origami patterns out of Si NMs using pre-stretched and pre-patterned PDMS substrates. The key parameter here is the shape of the pre-patterned PDMS walls. This approach is
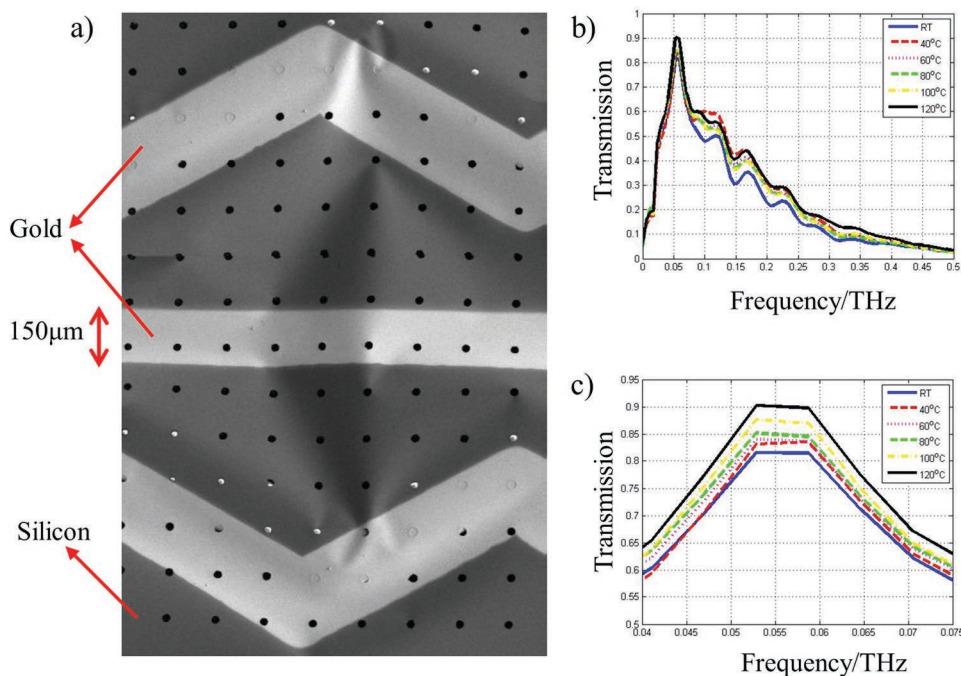
**Figure 3.** Transmission measurement of silicon (Si) nanomembrane (NM) "magic ball" pattern. a) An SEM image shows the gold antenna fabricated on Si NM. b) The measured transmission responses of proposed structure at temperatures of room temperature 24, 40, 60, 80, 100, and 120 °C, respectively. c) The zoom-in measured transmission responses of proposed structure at temperatures of 24, 40, 60, 80, 100, and 120 °C, respectively.

complementary to a recent work that is able to achieve 2D origami shapes where the creases are pre-defined by cutting, i.e., the concept of kirigami.[21,22] We demonstrated that this approach is able to mimic paper-based origami patterns and even modifies the paper-based origami for some non-rigidly foldable structures. Though the demonstrations are based on Si NWs, richer materials, such as metal and composites can be adopted to generate complex 3D architectures. To harness the tunability of the origami-based 3D architectures, one application on physically reconfigurable antenna has been demonstrated. We believe that the combination of origami-based microscale 3D architectures and antenna will lead to a breakthrough on physically and geometrically reconfigurable systems. As the described microscale Si origami has to be supported by a substrate, the application needs to focus on the responsive substrates, such as gels or shape memory polymers, for physically reconfigurable systems.

## Experimental Section

*Preparation of the Si NMs from SOI Wafer*: Si NM was prepared by patterning the top thin Si layer (300 nm in thickness) of an SOI wafer to form membranes ≈7 mm wide, 8 mm long with hole-arrays inside (8 µm in diameter for each hole) by reactive ion etching (Oxford Plasmalab 80 RIE Fluorine; $SF_6$, 100 W, 1 min) following photolithography (EVG 620, 300 mJ cm$^{-2}$) using photoresist (AZ 4330). Removing the photoresist with acetone and then etching the sacrifice $SiO_2$ layer with hydrofluoric acid (49%, 50 min) releases the membranes from the underlying Si substrate.

*Preparation of Elevated PDMS Walls on PDMS Stabs*: Silicon mold was made by a single side bare silicon wafer (500 µm in thickness), which was patterned with origami patterns by deep

silicon etching (STS ICP Advanced Silicon Etch, 75 min, 200 µm in depth) following photolithography (EVG 620, 400 mJ cm$^{-2}$) using photoresist (AZ 4330). The photoresist was then removed with acetone and a thin layer of release agent 1H,1H,2H,2H-perfluoro-octyltrichlorosilane was vapor-coated on top of the silicon. PDMS solution (mixed base and curing agent with 10:1 ratio by weight) was then poured into the mold and cure at 80 °C for 3 h. PDMS was peeled and cut into desire shape ≈20 mm wide, 15 mm long to serve as PDMS mold.

*Characterization of Microscale Silicon Origami*: Optical images were taken by Canon Eos 60D. SEM images were taken by focus ion beam (Nova 2000 NanoLab FEI). Optical profilometer images were taken using Zygo ZeScope. The Raman spectroscopy measurements were performed using a Renishaw InVia Raman microscope at 488 nm laser excitation source (laser power: 0.5 mW mm$^{-2}$) under 50× objective lens. The spectrum was fitted using Gaussian peak function.

*Finite Element Analysis*: The FEA was conducted using commercial finite element software package ABAQUS, and consists of two steps. The first step, mode analysis, or pre-buckling analysis, was carried out by calculating the eigenvalues of the model under the given loads and boundary conditions. The loads applied are simply in-plane equi-biaxial compressions which are equivalent to the uniform shrinkage due to the uniform decrease of temperature of the whole model. After the calculation, possible buckling shapes can be obtained. Then the static analysis, or post-buckling analysis, can be carried out since the post-buckling process is slow enough to be regarded as quasi-static. Same loads as above were applied in this step. The buckling modes obtained from previous step can be added to the initial geometry as the imperfection to trigger the buckling of the model. Finally, the stress and strain distribution of the buckling model can be obtained.

*Preparation of Antenna on Si NMs*: Shadow mask was first made by a bare silicon wafer (200 μm), which was patterned using photolithography to form zig-zag and ribbon structure, followed by deep silicon etching (STS ICP Advanced Silicon Etch, 75 min, 200 μm in depth). Si NMs were then physically covered with shadow mask and deposited 10 nm thick chrome and 300 nm thick gold layer successively by electron beam evaporation.

*THz Measurement Setup*: The THz-TDS transmission mode was used to measure these proposed samples. First, the samples were heated up using hot plate and then transferred quickly for transmission responses measurement at different temperatures: room temperature 24, 40, 60, 80, 100, and 120 °C, respectively. The IR thermometer was used to assure the temperature of the sample during all measurement.

## Supporting Information

Supporting Information is available from the Wiley Online Library or from the author.

## Acknowledgements

[1] M. C. Neyrinck, *Mon. Not. R. Astron. Soc.* **2012**, *427*, 494.
[2] S. M. Douglas, I. Bachelet, G. M. Church, *Science* **2012**, *335*, 831.
[3] P. W. Rothemund, *Nature* **2006**, *440*, 297.
[4] R. M. Zadegan, M. L. Norton, *Int. J. Mol. Sci.* **2012**, *13*, 7149.
[5] M. Nogi, N. Komoda, K. Otsuka, K. Suganuma, *Nanoscale* **2013**, *5*, 4395.
[6] Z. Song, T. Ma, R. Tang, Q. Cheng, X. Wang, D. Krishnaraju, R. Panat, C. K. Chan, H. Yu, H. Jiang, *Nat. Commun.* **2014**, *5*, DOI: 10.1038/ncomms4140.
[7] Z. Song, X. Wang, C. Lv, Y. An, M. Liang, T. Ma, D. He, Y.-J. Zheng, S.-Q. Huang, H. Yu, H. Jiang, *Sci. Rep.* **2015**, *5*, DOI: 10.1038/srep10988.
[8] R. Tang, H. Huang, H. Tu, H. Liang, M. Liang, Z. Song, Y. Xu, H. Jiang, H. Yu, *Appl. Phys. Lett.* **2014**, *104*, 083501.
[9] C. Lv, D. Krishnaraju, G. Konjevod, H. Yu, H. Jiang, *Sci. Rep.* **2014**, *4*, DOI: 10.1038/srep05979.
[10] J. L. Silverberg, A. A. Evans, L. McLeod, R. C. Hayward, T. Hull, C. D. Santangelo, I. Cohen, *Science* **2014**, *345*, 647.
[11] A. W. Topol, B. K. Furman, K. W. Guarini, L. Shi, G. M. Cohen, G. F. Walker, in *Proc. 54th Electronic Components and Technology Conf., 2004*, Vol. 1, IEEE, Las vegas, USA, **2004**.
[12] N. Dechev, L. Ren, W. Liu, W. L. Cleghorn, J. K. Mills, in *Proc. 2006 IEEE Int. Conf. Robotics and Automation, ICRA 2006*, IEEE, Orlando, USA, **2006**.
[13] A. Khademhosseini, R. Langer, J. Borenstein, J. P. Vacanti, *Proc. Natl. Acad. Sci. USA* **2006**, *103*, 2480.
[14] L. G. Griffith, M. A. Swartz, *Nat. Rev. Mol. Cell Biol.* **2006**, *7*, 211.
[15] H. Liang, T. Ma, C. Lv, H. Nguyen, G. Chen, H. Wu, R. Tang, H. Jiang, H. Yu, in *Proc. 64th IEEE Electronic Components and Technology Conf. (ECTC), 2014*, IEEE, Orlando, USA, **2014**.
[16] N. Bowden, S. Brittain, A. G. Evans, J. W. Hutchinson, G. M. Whitesides, *Nature* **1998**, *393*, 146.
[17] H. Zhang, X. Yu, P. V. Braun, *Nat. Nanotechnol.* **2011**, *6*, 277.
[18] J. G. Fernandez, A. Khademhosseini, *Adv. Mater.* **2010**, *22*, 2538.
[19] O. G. Schmidt, K. Eberl, *Nature* **2001**, *410*, 168.
[20] S. Xu, Z. Yan, K.-I. Jang, W. Huang, H. Fu, J. Kim, Z. Wei, M. Flavin, J. McCracken, R. Wang, A. Badea, Y. Liu, D. Xiao, G. Zhou, J. Lee, H. Chung, H. Cheng, W. Ren, A. Banks, X. Li, U. Paik, R. Nuzzo, Y. Huang, Y. Zhang, J. A. Rogers, *Science* **2015**, *347*, 154.
[21] Z. Yan, F. Zhang, J. Wang, F. Liu, X. Guo, K. Nan, Q. Lin, M. Gao, D. Xiao, Y. Shi, Y. Qiu, H. Luan, J. Kim, Y. Wang, H. Luo, M. Han, Y. Huang, Y. Zhang, J. A. Rogers, *Adv. Funct. Mater.* **2016**, *26*, 2629.
[22] Y. Zhang, Z. Yan, K. Nan, D. Xiao, Y. Liu, H. Luan, H. Fu, X. Wang, Q. Yang, J. Wang, W. Ren, H. Si, F. Liu, L. Yang, H. Li, J. Wang, X. Guo, H. Luo, L. Wang, Y. Huang, J. A. Rogers, *Proc. Natl. Acad. Sci. USA* **2015**, *112*, 11757.
[23] D. H. Gracias, V. Kavthekar, J. C. Love, K. E. Paul, G. M. Whitesides, *Adv. Mater.* **2002**, *14*, 235.
[24] X. Guo, H. Li, B. Y. Ahn, E. B. Duoss, K. J. Hsia, J. A. Lewis, R. G. Nuzzo, *Proc. Natl. Acad. Sci. USA* **2009**, *106*, 20149.
[25] J. Cho, M. D. Keung, N. Verellen, L. Lagae, V. V. Moshchalkov, P. V. Dorpe, D. H. Gracias, *Small* **2011**, *7*, 1943.
[26] J. A. Rogers, Y. Huang, O. G. Schmidt, D. H. Gracias, *MRS Bull.* **2016**, *41*, 123.
[27] D. C. Duffy, J. C. McDonald, O. J. Schueller, G. M. Whitesides, *Anal. Chem.* **1998**, *70*, 4974.
[28] D.-Y. Khang, H. Jiang, Y. Huang, J. A. Rogers, *Science* **2006**, *311*, 208.
[29] Y. Sun, W. M. Choi, H. Jiang, Y. Y. Huang, J. A. Rogers, *Nat. Nanotechnol.* **2006**, *1*, 201.
[30] K. Miura, presented at *Proc. 31st Congress Int. Astronautical Federation*, IAF, Tokyo, Japan, **1980**.
[31] T. C. Hull, *Linear Algebra Appl.* **2002**, *348*, 273.
[32] S.-M. Belcastro, T. C. Hull, in *Origami3: Proceedings of the 3rd International Meeting of Origami Mathematics, Science, and Education* (Ed: Thomas Hull), CRC Press, Natick, MA, **2002**.
[33] V. Sanphuang, W.-G. Yeo, J. L. Volakis, N. K. Nahar, *IEEE Trans. THz Sci. Technol.* **2015**, *5*, 117.

## Microscale Silicon Origami

*Zeming Song, Cheng Lv, Mengbing Liang, Varittha Sanphuang, Kedi Wu, Bin Chen, Zhi Zhao, Jing Bai, Xu Wang, John L. Volakis, Liping Wang, Ximin He, Yu Yao, Sefaattin Tongay, and Hanqing Jiang\**

# WILEY-VCH

# Supporting Information

**Microscale Silicon Origami**

By *Zeming Song[#], Cheng Lv[#], Mengbing Liang, Varittha Sanphuang, Kedi Wu, Bin Chen, Zhi Zhao, Jing Bai, Xu Wang, John L. Volakis, Liping Wang, Ximin He, Yu Yao, Sefaattin Tongay,* and *Hanqing Jiang\**

**[#]These authors contribute equally.**

[*]     Prof. Hanqing Jiang
School for Engineering of Matter, Transport and Energy, Arizona State University, Tempe, AZ, 85287 (USA)
E-mail: hanqing.jiang@asu.edu
        Dr. Zeming Song, Cheng Lv, Kedi Wu, Bin Chen, Dr. Zhi Zhao, Xu Wang, Prof. Liping Wang, Prof. Ximin He, and Prof. Sefaattin Tongay
School for Engineering of Matter, Transport and Energy, Arizona State University, Tempe, AZ, 85287 (USA)
        Mengbing Liang, Jing Bai, Prof. Yu Yao
School of Electrical, Computer and Energy Engineering, Arizona State University, Tempe, AZ, 85287 (USA)
        Varittha Sanphuang and Prof. John L. Volakis
ElectroScience Laboratory, Department of Electrical and Computer Engineering, The Ohio State University, Columbus, OH, 43212 (USA)

Keywords: Origami, Silicon nanomambrane, PDMS, Reconfigurable antenna

**1. Silicon (Si) nanomembranes (NMs) Miura-ori patterns**

The detailed geometry of the pre-patterned PDMS wall is given in Figure S1a and S1b. Figure S1c and S1d provide a cross-sectional view near the elevated PDMS walls using an integrated focused ion beam (FIB) and an SEM system, where the partial delamination is observed at the corner of the elevated PDMS wall that defines a Miura-ori pattern.
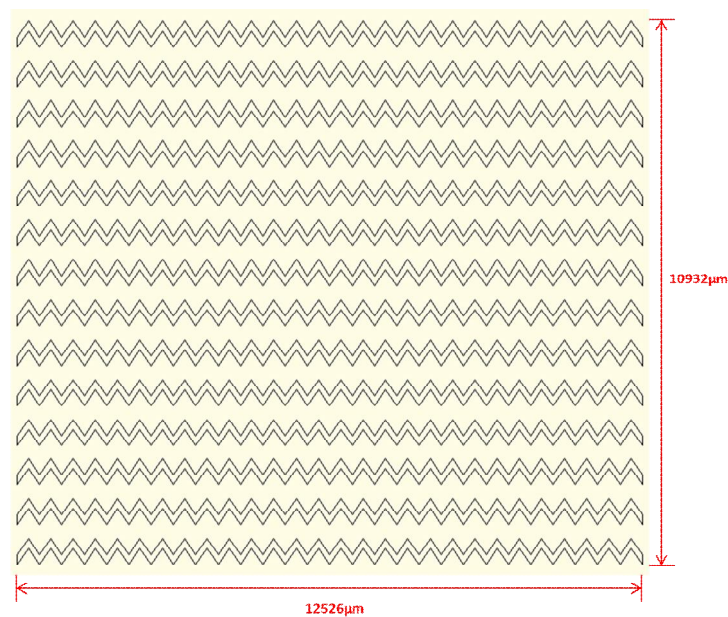


(a)
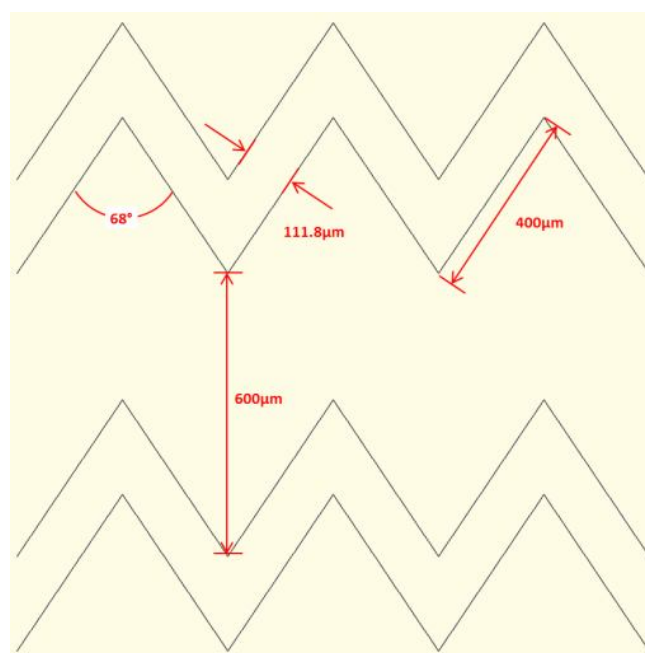
(b)
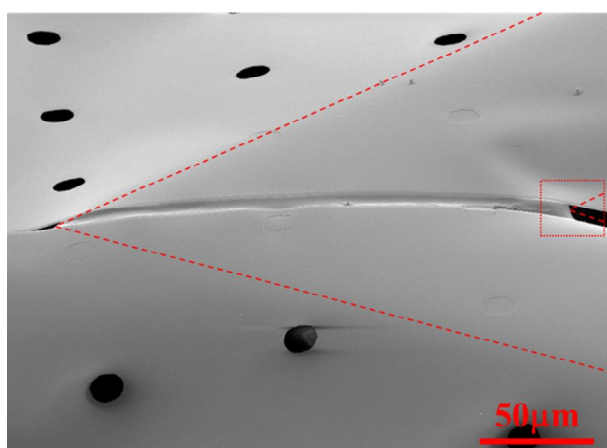


(c)
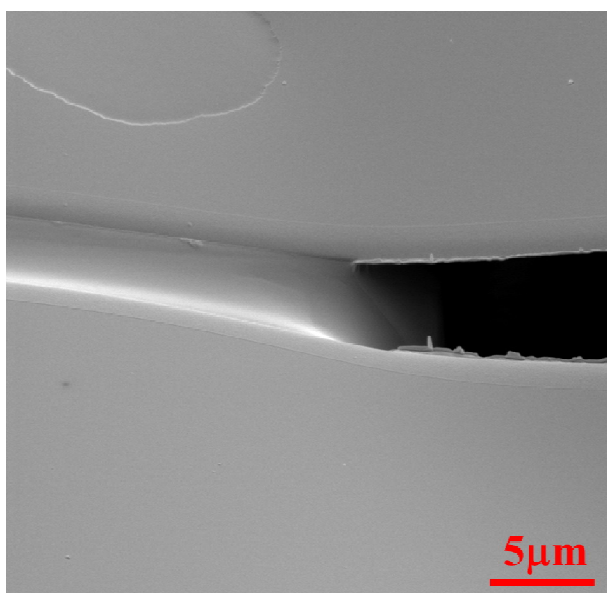


(d)

Figure S1. Geometry of the pre-patterned PDMS wall with Miura-ori pattern. (a) Overall dimension. (b) Detailed dimension. (c) and (d) SEM images near the elevated PDMS walls. Triangular dash lines in (c) indicate creases and in ractangular dash lines is the delamination region and has been zoomed in in (d).

## 2. Analytical solution for Miura-ori pattern

Figure S2a and S2b show the 3D view and the top view of the unit cell of a Miura-ori pattern. The origin of stationary coordinate system is "O". Due to the biaxial compressive strain $\varepsilon$ (<0), the overall strain of the pattern in y-direction due to the biaxial compression is $\varepsilon$, thus the stretch ratio in y-direction is $\lambda = 1 - \varepsilon$. The length of line $BC$ and $AB$ are assumed to be $a$ and $b$, respectively. The angle $\angle ABC$ is denoted as $\beta$. Then we can obtain the vector $\overrightarrow{OA} = \left(0, -a\lambda, -a\sqrt{1-\lambda^2}\right)$, and $\overrightarrow{OC} = \left(b\sqrt{1-\left[\cos\beta/\lambda\right]^2}, -b\cos\beta/\lambda, 0\right)$. The normal vector of the plane OABC is then $\mathbf{n} = \overrightarrow{OA} \times \overrightarrow{OC}$. As the origin O is in this plane, the equation of the plane can be shown as: $A_1 x + A_2 y + A_3 z = 0$ ( $0 < x < B_2$, $B_1 x / B_2 - a\lambda < y < B_1 x / B_2$ ), where $A_1 = -ab\sqrt{1-\lambda^2}\cos\beta/\lambda$, $A_2 = -ab\sqrt{\left(1-\lambda^2\right)\left[1-\left(\cos\beta/\lambda\right)^2\right]}$, $A_3 = ab\lambda\sqrt{1-\left(\cos\beta/\lambda\right)^2}$, $B_1 = -\left(b\cos\beta\right)$, and $B_2 = b\sqrt{1-\left(\cos\beta/\lambda\right)^2}$.

Similarly, the equation of the plane OCDE is: $-A_1 x - A_2 y + A_3 z = 0$ ( $0 < x < B_2$, $B_1 x / B_2 < y < B_1 x / B_2 + a\lambda$ ). The equation of the plane OAFG is: $-A_1 x + A_2 y + A_3 z = 0$ ( $-B_2 < x < 0$ $-B_1 x / B_2 - a\lambda < y < -B_1 x / B_2$ ). The equation of the plane OEGH is: $A_1 x - A_2 y + A_3 z = 0$ ( $0 < x < B_2$, $-B_1 x / B_2 < y < -B_1 x / B_2 + a\lambda$ ).

In both FEA and the experiment, we have the following dimensions: $a = 400\,\mu m$ (include the dimension of wall on y-direction), $b = 400\,\mu m$, $\beta = 34°$, $\lambda = 96.4\%$. Then we can obtain the constants as: $A_1 = -36588$, $A_2 = -21710$, $A_3 = 78708$, $B_1 = 331.6150$, $B_2 = -204.1193$. For the line cut by the $yz$-plane, we need only to solve the equations:

$$\begin{cases} A_1x + A_2y + A_3z = 0 \\ x = 0 \end{cases} \text{ for line EO and } \begin{cases} -A_1x - A_2y + A_3z = 0 \\ x = 0 \end{cases} \text{ for line OA.}$$

After proper offset, we can obtain the theoretical profile for Miura-ori in y-direction, which is shown in Figure 1. Similarly, the other two profiles for Miura-ori can be obtained.
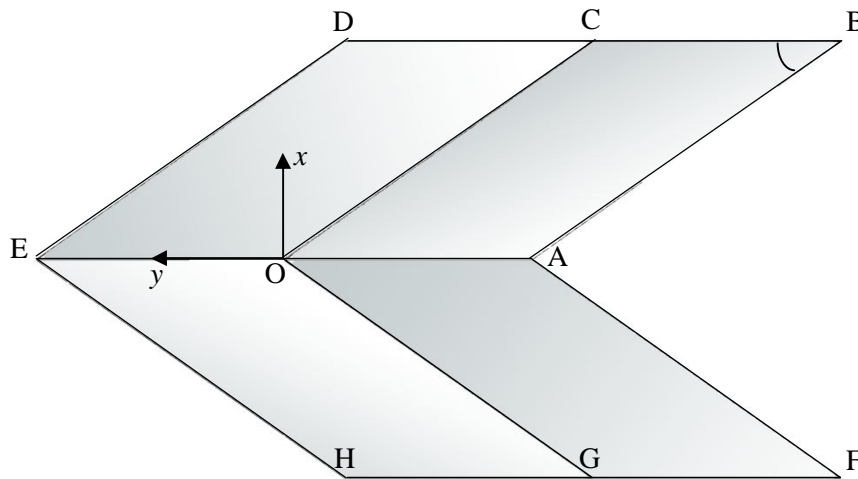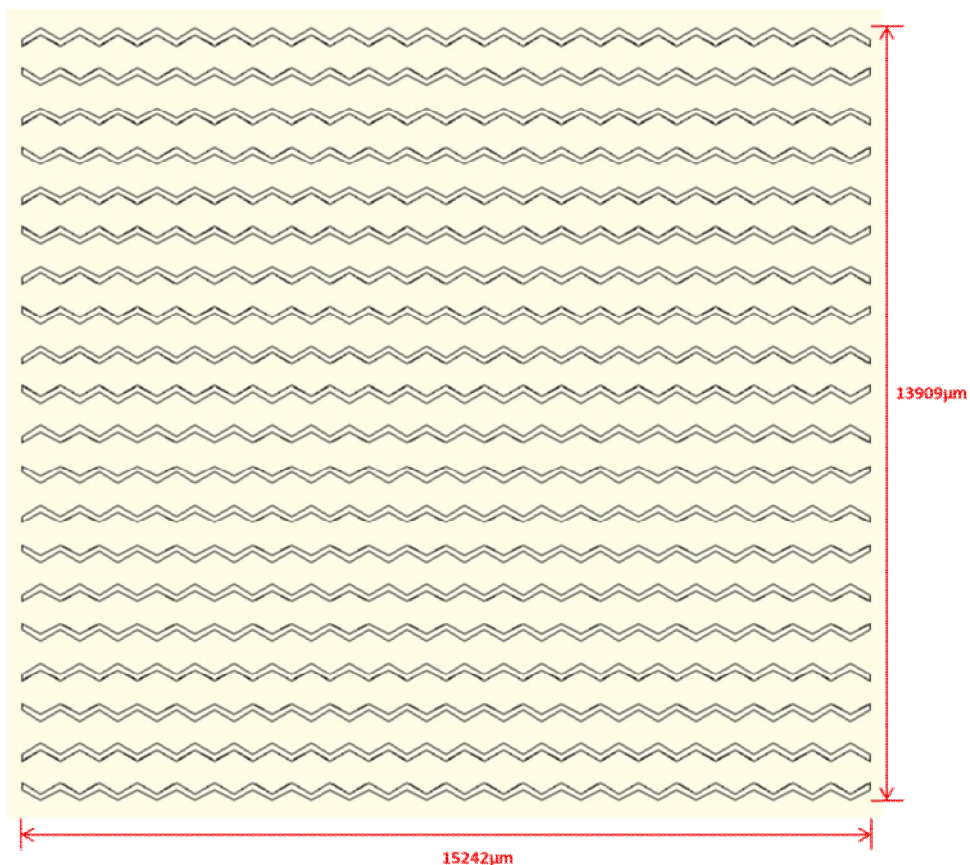


(a)
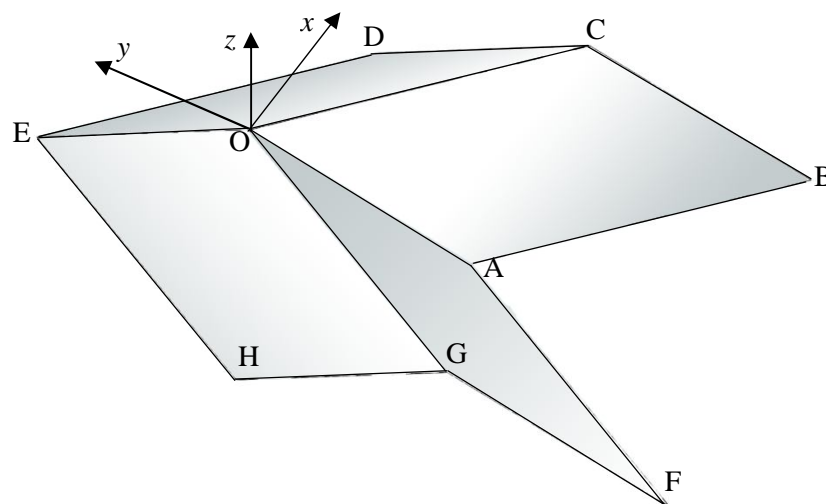


(b)

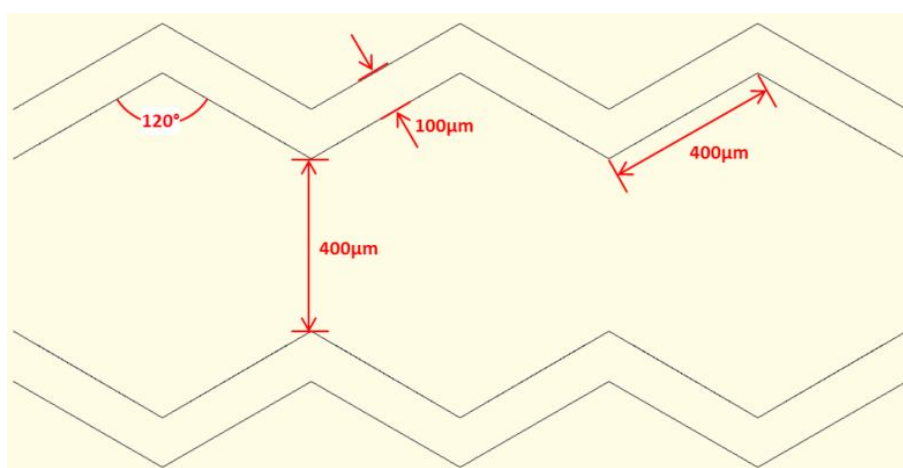Figure S2. Analytical geometry of a unit cell for Miura-ori pattern. (a) Top view. (b) Perspective view.

**3. Silicon (Si) nanomembranes (NMs) "magic ball" patterns**

The detailed geometry of the pre-patterned PDMS wall is given in Figure S3a and S3b.



(a)



(b)

Figure S3. Geometry of the pre-patterned PDMS wall with magic ball pattern. (a) Overall dimension. (b) Detailed dimension.

## 4. Analytical solution for "magic ball" pattern

3D view and the cross section view (cut along the plane COF) of the unit cell of the ‚magic ball" pattern are shown in Figure S4a and S4b. The origin of stationary coordinate system is "O". Assuming we know the overall strain $\varepsilon$ of the pattern in x-direction due to the biaxial compression, the stretch ratio in x-direction is $\lambda = 1 - \varepsilon$. The length of line $BC$ and $OC$ are assumed to be $a$ and $b$, respectively. Then we can obtain the vector

$$\overrightarrow{OC} = \left(0, a\sin\theta, a\cos\theta\right) \quad , \quad \overrightarrow{OB} = \left(-a\lambda, b, a\sqrt{1-\lambda^2}\right) \quad , \quad \text{where,}$$

$\theta = \arctan\left(1/\sqrt{1-\lambda^2}\right) - \arctan\left(\sqrt{1-\lambda^2}\right)$. The normal vector of the plane OBC is then $\mathbf{n} = \overrightarrow{OC} \times \overrightarrow{OB}$. As the origin O is in this plane, the equation of the plane can be shown as:

$C_1 x + C_2 y + C_3 z = 0$ ( $x < 0$ , $bx + a\lambda y > 0$ , $\left(b - a\sin\theta\right)x + a\lambda\left(y - a\sin\theta\right) < 0$ ), where,

$C_1 = a^2\sin\theta\sqrt{1-\lambda^2} - ab\cos\theta$ , $C_2 = a^2\lambda\cos\theta$ , $C_3 = -a^2\lambda\sin\theta$ .

Similarly, the equation of the plane OCD is: $-C_1 x + C_2 y + C_3 z = 0$ ( $x > 0$ , $-bx + a\lambda y > 0$ , $\left(b - a\sin\theta\right)x - a\lambda\left(y - a\sin\theta\right) > 0$ ). The equation of the plane ODE is: $\sqrt{1-\lambda^2}x - \lambda z = 0$ ( $x < a\lambda$ , $-bx + a\lambda y < 0$ 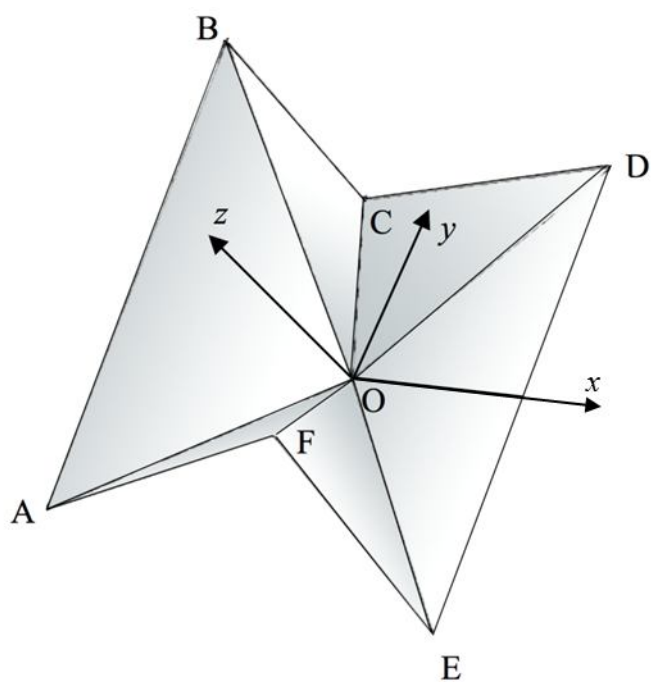, $bx + a\lambda y > 0$ ). The equation of the plane OEF is: $-C_1 x - C_2 y + C_3 z = 0$ ( $x > 0$ , $bx + a\lambda y < 0$ , $\left(b - a\sin\theta\right)x + a\lambda\left(y + a\sin\theta\right) > 0$ ). The equation of the plane OAF is: $C_1 x - C_2 y + C_3 z = 0$ ( $x < 0$ , $-bx + a\lambda y < 0$ , $\left(b - a\sin\theta\right)x - a\lambda\left(y + a\sin\theta\right) < 0$ ). The equation of the plane OAB is: $\sqrt{1-\lambda^2}x + \lambda z = 0$ ( $x > -a\lambda$ , $-bx + a\lambda y > 0$ , $bx + a\lambda y < 0$ ).

In the experiment, we have the following dimensions: $a = 400\,\mu m$ , $b = 457.735\,\mu m$ (include the dimension of wall on y-direction), $\lambda = 96.4\%$ . Then we can obtain the constants as: $\theta = 60.22°$ , $C_1 = -54015$ , $C_2 = 76609$ , $C_3 = 133870$ .

(a)
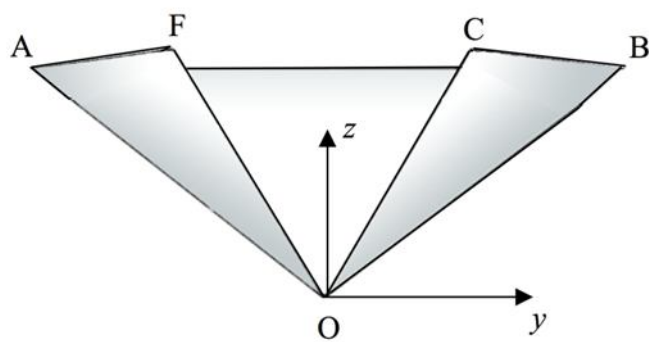


(b)

Figure S4. Analytical geometry of a unit cell for waterbomb pattern. (a) Perspective view.

(b) Side view.

**5. Raman spectroscopy measurements for silicon (Si) nanomembrane (NM) "magic ball" pattern**

The amount of strain carried by remarkably curved parts of our designed Si origami pattern is established via Raman Spectroscopy measurements. Specifically, the temperature dependence of lattice parameter as well as vibrational property, characterized by Raman Spectroscopy, of Si has been studied since the 1960's[1-3]. Taking advantage of temperature as an intermediary, the variation of lattice parameter can be predicted by the shifting of Raman peak position, and the strain amount can be directly calculated by strain (%) = ($a$ − $a_0$)/$a_0$×100%, where $a_0$ and $a$ are lattice parameters before and after applied deformation, respectively. Therefore, the applied strain can be quantized by Raman peak position, as is shown in Figure S5a. Here, we measured the Raman spectrum of the exceedingly bended tip, which is marked by a red triangle in Figure 2b, and the corresponding spectrum is shown in Figure S5b. Instead of an obvious shifting, the measured spectrum at the tip (red solid line) appears much broader than that of flat Si. This is a result of the fact that our incident laser can also hit some unstrained part of the lattice, and thus the measured Raman spectrum represents for a combination of both strained and unstrained parts of the Si origami pattern. Here, the measured peak center position is located at 518 cm$^{-1}$, representing an average strain of 0.05%. To further explore the maximum strain, the measured peak is fitted into two peaks located at 521 cm$^{-1}$ and 515 cm$^{-1}$, representing for unstrained and strained part, respectively. Thus, the highest strain amount reaches as much as 0.1 %. Therefore, the strain value ranges from 0 to 0.1% with an average value of 0.05%.
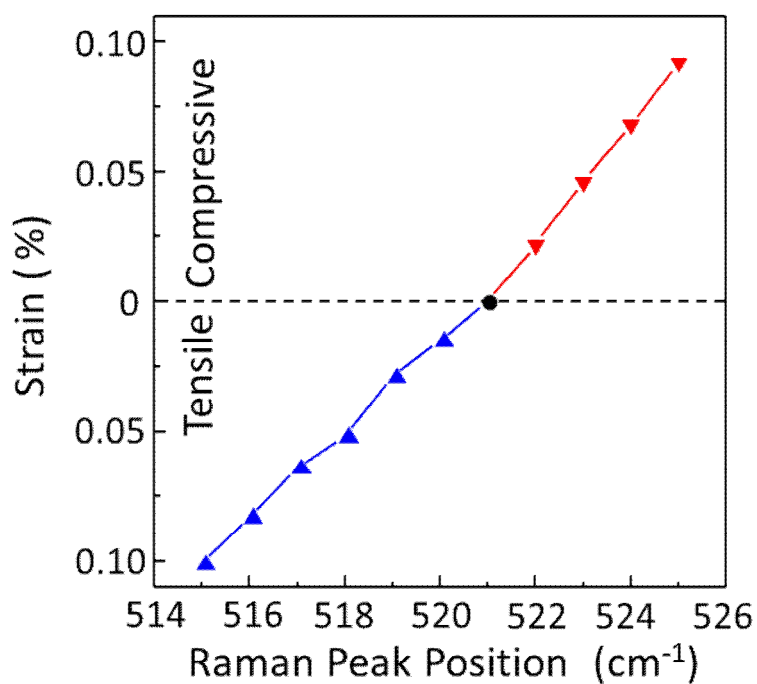
(a)
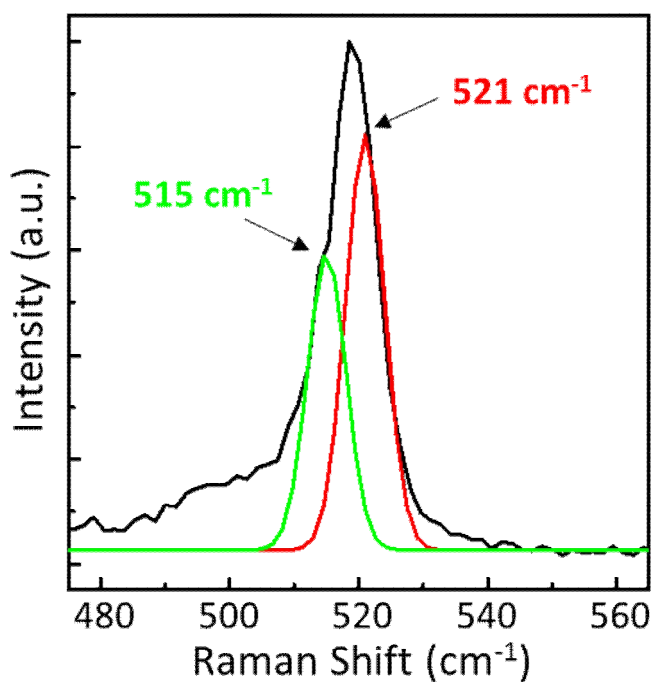


(b)

Figure S5. The quantization of strain on Si NMs with magic ball structure by Raman Spectroscopy (a) The dependence of strain verse Raman peak position of Silicon. (b) Raman spectra of measured spot, and fitted peaks (green and red).

## 6. Silicon (Si) nanomembranes (NMs) non-rigidly foldable patterns

The detailed geometry of the pre-patterned PDMS wall is given in Figure S6a and S6b.
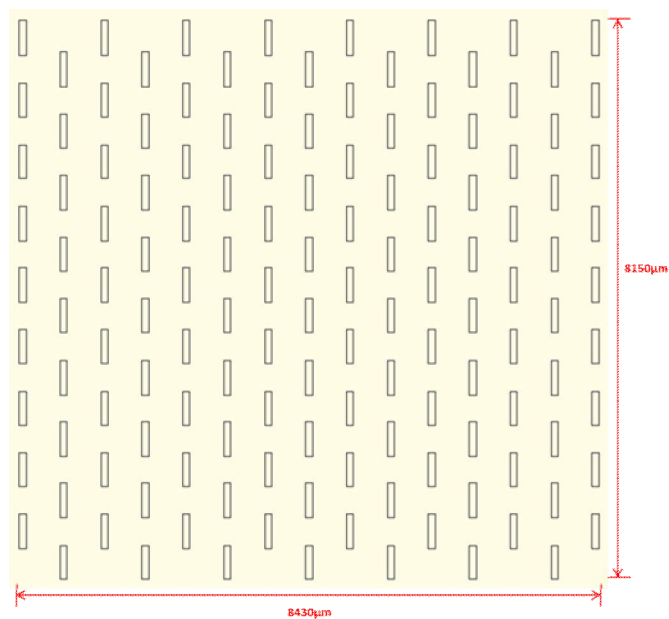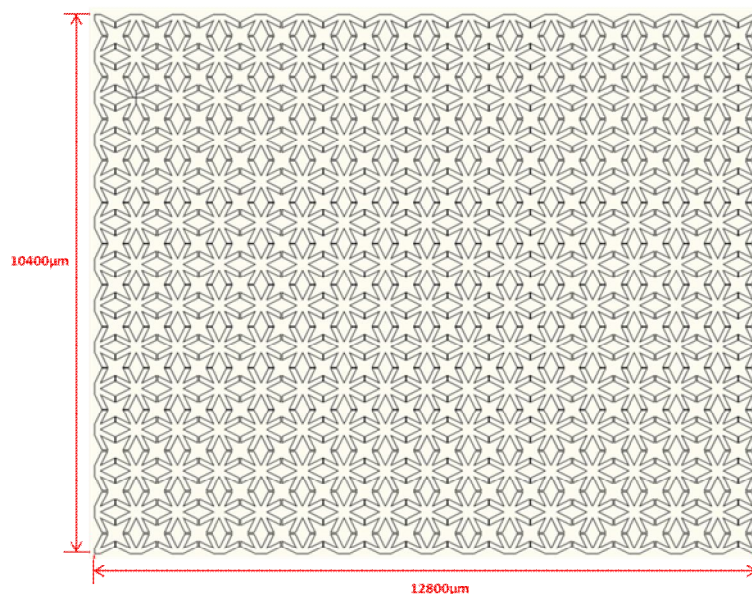


(a)
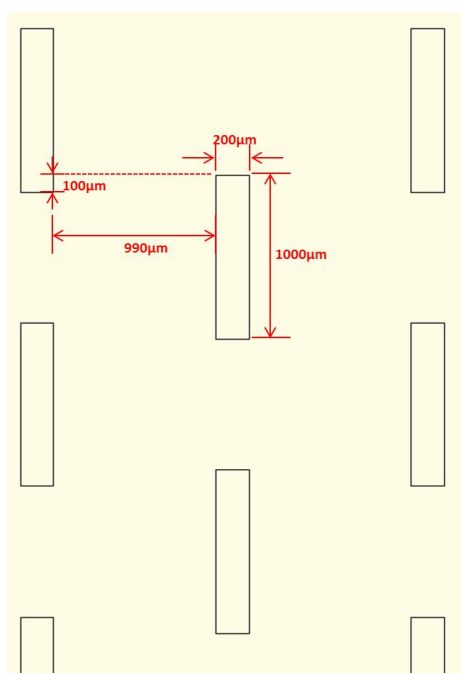


(b)

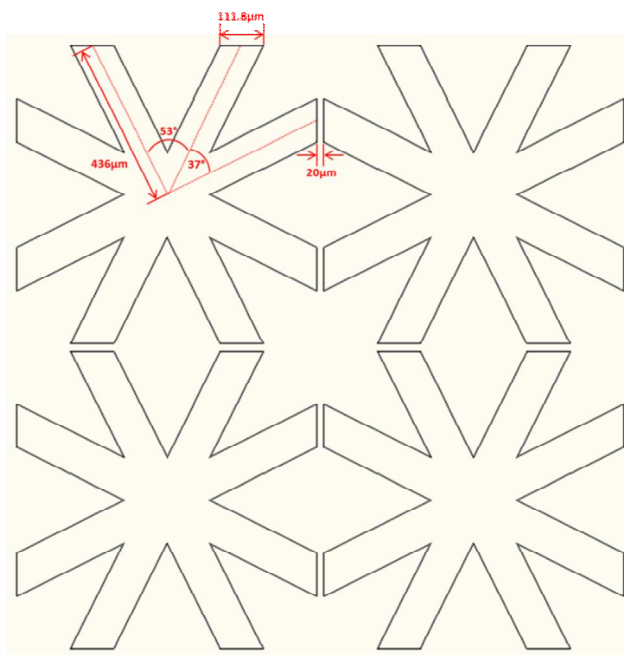Figure S6. Geometry of the pre-patterned PDMS wall with non-rigidly foldable pattern. (a) Overall dimension. (b) Detailed dimension.

**7. Silicon (Si) nanomembranes (NMs) stars pattern**

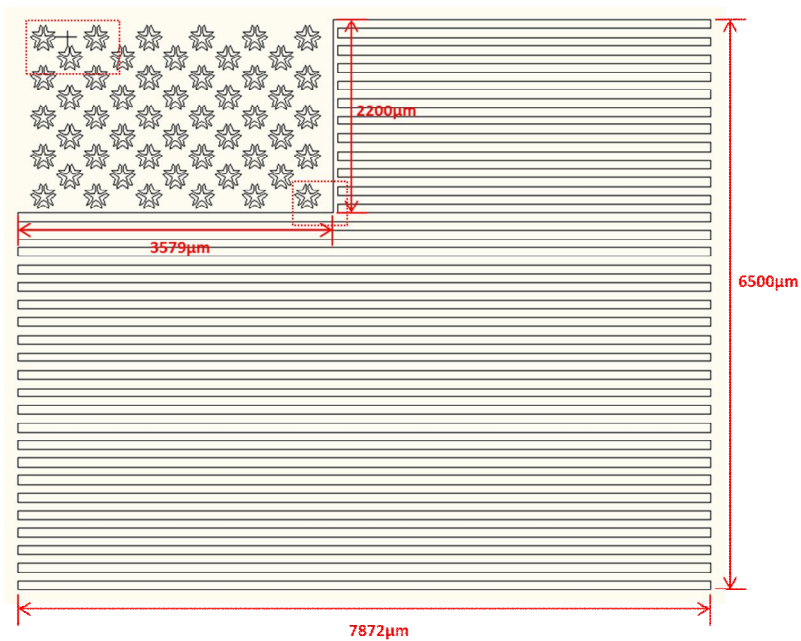The detailed geometry of the pre-patterned PDMS wall is given in Figure S7a and S7b.



(a)



(b)

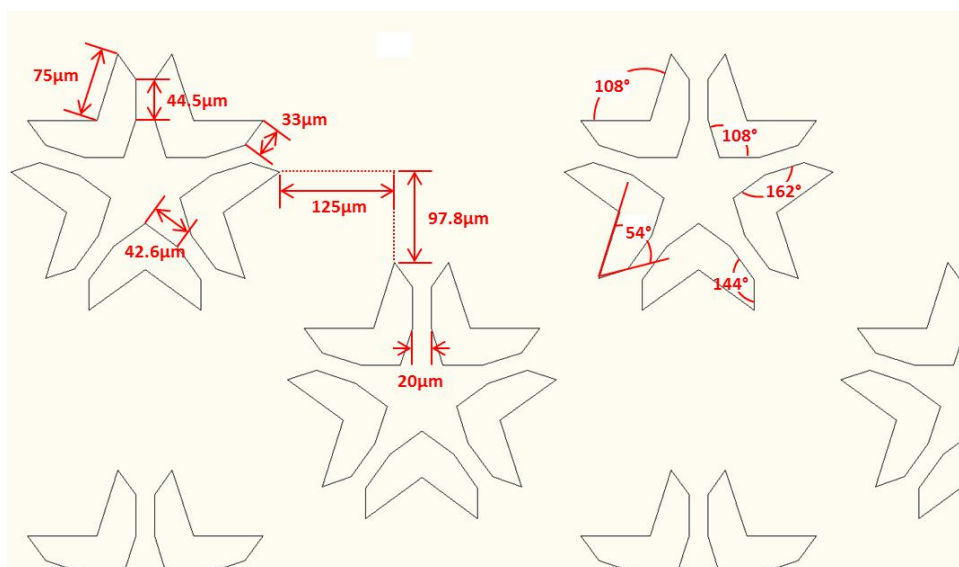Figure S7. Geometry of the pre-patterned PDMS wall with star pattern. (a) Overall dimension.

(b) Detailed dimension.

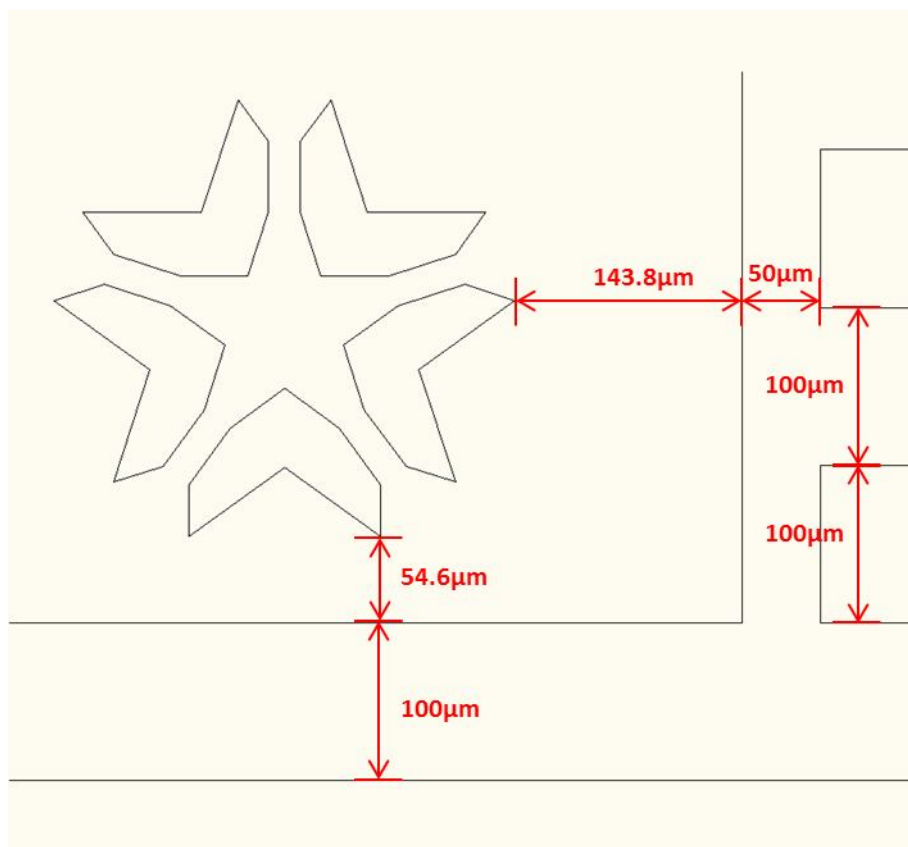## 8. Silicon (Si) nanomembranes (NMs) US Flag pattern

The detailed geometry of the pre-patterned PDMS wall is given in Figure S8a and S8b.



(a)



(b)

13

(c)

Figure S8. Geometry of the pre-patterned PDMS wall with US flag pattern. (a) Overall dimension. (b) Detailed dimension. (c) Detailed dimension near the boundary of star pattern and strip pattern.

## 9. Principle of THz measurement

The transmission characterization was done using a time domain THz spectroscopy (TPS3000, TeraView Ltd.) see Figure S9 at normal angle of incidence ($\theta = 0^\circ$). The schematics of THz time domain spectrometer (THz-TDS) in transmission mode is illustrated in Figure. S9. The broadband THz pulses are achieved by the emission of photoconductive antenna through optical excitation by an ultrafast, pulsed near-infrared laser, which covers a frequency range of 0.06 THz to 3 THz. Note that the spectral resolution of this system is 0.0075 THz. The incident terahertz wave radiated from the emitter is transmitted as a focus beam through the sample before detection. Note that the transmitted signal through air is used as the reference signal throughout this study.
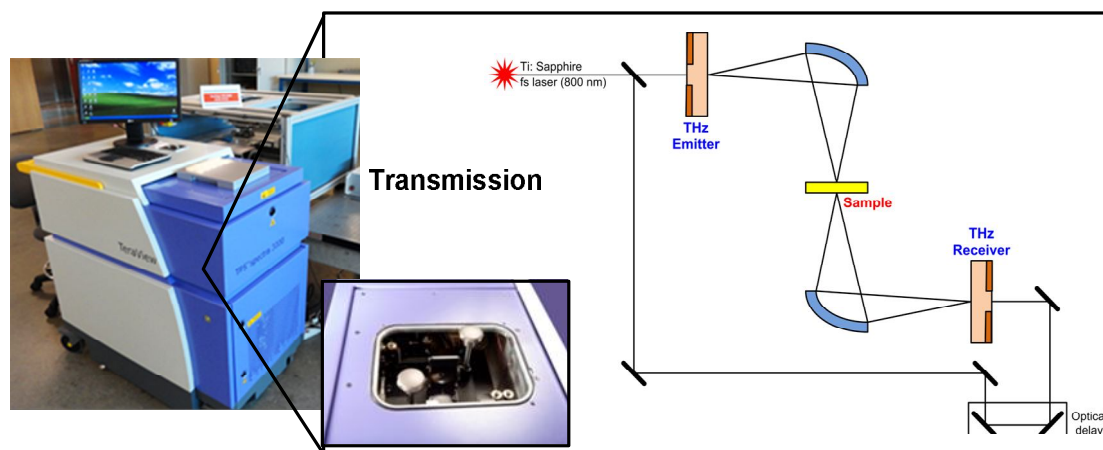


Figure S9. Schematics of THz time domain spectrometer (THz-TDS): TPS3000, Teraview Ltd. in transmission mode.

Reference

[1]    R. Hall, *Acta Crystallogr.* **1961**, *14*, 1004.

[2]    Y. Okada, Y. Tokumaru, *J. Appl. Phys.* **1984**, *56*, 314.

[3]    T. Hart, R. Aggarwal, B. Lax, *Phys. Rev. B* **1970**, *1*, 638.